

Optical Engineering

SPIDigitalLibrary.org/oe

Review of superconducting nanowire single-photon detector system design options and demonstrated performance

Eric A. Dauler
Matthew E. Grein
Andrew J. Kerman
Francesco Marsili
Shigehito Miki
Sae Woo Nam
Matthew D. Shaw
Hirotaka Terai
Varun B. Verma
Taro Yamashita

Review of superconducting nanowire single-photon detector system design options and demonstrated performance

Eric A. Dauler,^{a,*} Matthew E. Grein,^a Andrew J. Kerman,^a Francesco Marsili,^b Shigehito Miki,^c Sae Woo Nam,^d Matthew D. Shaw,^b Hirotaka Terai,^c Varun B. Verma,^d and Taro Yamashita^c

^aMIT Lincoln Laboratory, 244 Wood Street, Lexington, Massachusetts 02420

^bJet Propulsion Laboratory, California Institute of Technology, 4800 Oak Grove Dr., Pasadena, California 91109

^cKobe Advanced Research Center, National Institute of Information and Communications Technology, 588-2, Iwaoka, Iwaoka-cho, Nishi-ku, Kobe, Hyogo, Japan 651-2492

^dNational Institute of Standards and Technology, 325 Broadway, Boulder, Colorado 80305

Abstract. We describe a number of methods that have been pursued to develop superconducting nanowire single-photon detectors (SNSPDs) with attractive overall performance, including three systems that operate with >70% system detection efficiency and high maximum counting rates at wavelengths near 1550 nm. The advantages and tradeoffs of various approaches to efficient optical coupling, electrical readout, and SNSPD design are described and contrasted. Optical interfaces to the detectors have been based on fiber coupling, either directly to the detector or through the substrate, using both single-mode and multimode fibers with different approaches to alignment. Recent advances in electrical interfaces have focused on the challenges of scalability and ensuring stable detector operation at high count rates. Prospects for further advances in these and other methods are also described, which may enable larger arrays and higher-performance SNSPD systems in the future. Finally, the use of some of these techniques to develop fully packaged SNSPD systems will be described and the performance available from these recently developed systems will be reviewed. © The Authors. Published by SPIE under a Creative Commons Attribution 3.0 Unported License. Distribution or reproduction of this work in whole or in part requires full attribution of the original publication, including its DOI. [DOI: [10.1117/1.OE.53.8.081907](https://doi.org/10.1117/1.OE.53.8.081907)]

Keywords: photodetectors; detector arrays; quantum efficiency; optoelectronic packaging.

Paper 140298SSV received Feb. 20, 2014; revised manuscript received Apr. 3, 2014; accepted for publication Apr. 11, 2014; published online Jun. 16, 2014.

1 Introduction

Significant advances have been made in superconducting nanowire single-photon detectors (SSPDs or SNSPDs) since their initial demonstration.¹ These detectors can enable high-speed single-photon detection over a wide range of ultraviolet to infrared wavelengths with high detection efficiency (DE), low noise, and precise photon timing. In addition to advances in the device physics, detector design, and applications,² progress has also been made in translating high-performance SNSPD devices into complete systems that provide users with access to those detector capabilities.³⁻⁵ In particular, progress in low-loss optical coupling, improved readout circuits, and optimized device designs have allowed the demonstration of detector systems that simultaneously offer high system DE, high maximum count rates, low noise, and low timing jitter. A number of different engineering approaches have been used to overcome these challenges and each technique offers advantages and tradeoffs in terms of implementation complexity, performance, and scalability.

This review is divided into three sections that describe a number of approaches that have been pursued for the optical and electrical interfaces and some of the high-performance systems that have been demonstrated. In Sec. 2, techniques for efficiently coupling light into the detectors are described. In order to achieve high system DE, this optical coupling must have low loss and precisely align the desired optical

modes onto the relatively small active area of an SNSPD (typically 10 to 20 μm in diameter). Furthermore, this optical coupling must limit the blackbody radiation and other sources of optical background from heating or generating noise counts in the detector. In Sec. 3, techniques for electrical readout are detailed. The electrical interface to each SNSPD element must provide a (1) high-frequency impedance that permits the desired detector operation and reset behavior, (2) low-noise bias current, and (3) high-speed output that supports the required timing resolution, signal-to-noise ratio, and count rates. Finally, an overall system must be developed that integrates a suitably optimized SNSPD or array of SNSPD elements with the desired optical and electrical interfaces. Section 4 will describe three systems³⁻⁵ that incorporate different SNSPDs and interfaces to provide high-performance single-photon detection systems.

2 Optical Interfaces

2.1 Direct Fiber-Coupling to the Detector

Standard telecommunication single-mode fibers (SMFs) provide a well-defined and flexible optical input that inherently filters a large fraction of the room-temperature blackbody radiation. A method for precisely aligning these fibers to detectors on silicon substrates using silicon micromachining and standard optical components was originally developed at National Institute of Standards and Technology (NIST) for transition edge sensors⁶ and has more recently been adapted

*Address all correspondence to: Eric A. Dauler, E-mail: edauler@LL.mit.edu

for SNSPDs by NIST and the Jet Propulsion Laboratory.³ This method allows (1) sub-Kelvin operating temperatures, (2) no moving parts at low temperatures, (3) fast assembly with no manual alignment, (4) compact packaging of many detectors in a limited cryogenic volume, and (5) exploitation of low-cost commercial, off-the-shelf components.

This technique was used to align single-mode telecommunication fibers to tungsten silicide (WSi) SNSPDs that were fabricated on thermally oxidized 3-in. Si wafers as described in Ref. 3. The detectors were embedded in an optical stack to enhance the absorption of the nanowires. The optical stack was composed of the following layers from top (illumination side) to bottom (substrate side): TiO₂, SiO₂, WSi nanowires, SiO₂, and Au, which required depositing a high-quality, superconducting WSi film at low temperature on top of SiO₂ and Au. The nanowires were 4 to 5 nm thick, 100 to 200 nm wide, and the fill factor (the ratio between the width and the pitch of the nanowires) was varied from 50 to 65%. Figure 1(a) shows the active area of a WSi SNSPD, which was circular and had a diameter of 15 μm . The last step of the fabrication process of the detectors was a Bosch dry-etch process, which defined keyhole-shaped dies through the Si wafer, as shown in Fig. 1(b). The detectors were placed in the center of the round parts of the dies that have a diameter that closely matches the inner diameter (2.5 mm) of the zirconia alignment sleeve. Figure 1(c) shows the optical alignment assembly: (1) standard telecommunication SMF terminated with a zirconia ferrule, (2) zirconia alignment sleeve, (3) device die, and (4) back-side sapphire ferrule. The alignment of the $\sim 9\text{-}\mu\text{m}$ -diameter core of the fiber to the active area of the SNSPD was ensured by the precise dimensions of the detector die, the fiber ferrule, and the alignment sleeve. The precision of this alignment scheme has been estimated to be $\sim 3\ \mu\text{m}$.⁶

The rectangular neck of the detector die routed the device wiring out of the zirconia alignment sleeve to enable wire bonding to the machined metal chip holder. The back-side sapphire ferrule was press-fitted into a machined hole to capture the sleeve and to provide thermal contact between the zirconia components and the cooled metal components. Figure 1(d) shows the assembled detector package, which had a volume of $\sim 0.3\ \text{cm}^3$.

2.2 Fiber-Coupling Using Fusion-Spliced Graded Index Lenses

Although the lithographic approach to fiber alignment described in Sec. 2.1 has many advantages, the near-contact between the optical fiber and the SNSPD does place constraints on the detector structures and layout. These constraints include (1) a substrate material suitable for deep etching, (2) the need for a reflector between the substrate and the nanowires in order to achieve near-unity absorption in the detector, and (3) the need to avoid the relatively large fiber ferrule when routing electrical connections. These three constraints can be alleviated by coupling light through the substrate material. However, some combination of a short optical path length (thin substrate) or a lens to focus the light is required to couple light into the small area of typical SNSPDs. In this section, an approach to use compactly packaged focusing optics is discussed.

A schematic layout is shown in Fig. 2(a) for the fiber-coupled packaging used to align optical components to a back-illuminated SNSPD (in which a reflector is fabricated on top of the nanowire detector and optical illumination is through the substrate).⁷ A fiber ferrule was fixed to the fiber-holding block in advance by using an adhesive so that the distance from the exit end to the rear surface of the SNSPD chip was 20 μm . SNSPD chips were mounted

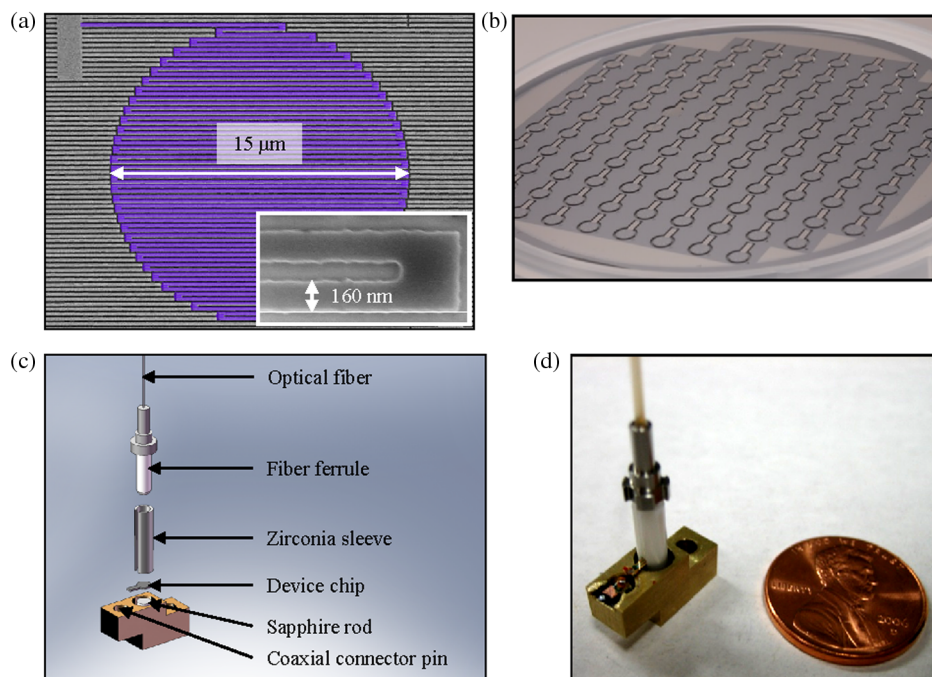


Fig. 1 (a) Scanning electron microscope (SEM) image of the active area and of the nanowires (inset) of WSi superconducting nanowire single-photon detectors (SNSPDs). (b) Detector wafer. (c) Schematic representation of the optical alignment assembly. (d) Assembled detector package.

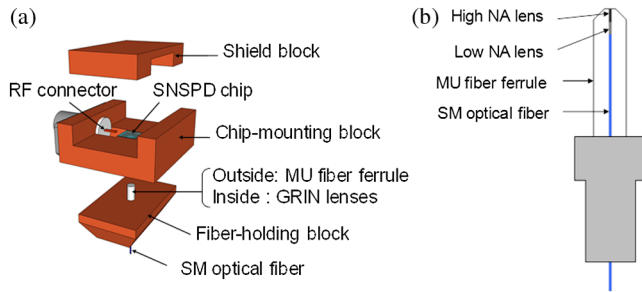


Fig. 2 (a) Schematic layout for the fiber-coupled SNSPD package. (b) Configuration of gradient index lenses connected to the optical fiber.

on chip-mounting blocks, which had a through hole at the center of the chip-mounting area to insert a fiber ferrule. The fiber-holding block was joined to the chip-mounting block from the rear, and the two blocks were accurately aligned so that the incident light spot illuminated the center of the meander area. The dimensions of the packaging blocks are 15 mm (length) \times 15 mm (width) \times 10 mm (thickness), which are sufficiently compact to install multiple packages into a Gifford-McMahon (GM) cryocooler system.

To achieve efficient optical coupling, small gradient index (GRIN) lenses were used to reduce the beam waist at a distance from the exit-end. To embed lenses into the compact packages, GRIN lenses with a diameter of 125 μm , which is equal to the cladding diameter of a single-mode optical fiber, are directly fusion-spliced to the end of the optical fiber. Since the fiber-spliced lenses were inserted into the miniature-unit (MU) fiber ferrule, the shape of the end of the fiber did not change at all from that without lenses, as shown in Fig. 2(b). The numerical aperture and length of the two lenses are chosen so that the working distance is equal to the optical path length (between the end of the fiber and the device active area in the package) and the beam waist becomes as small as possible. For example, the beam waist ($2\omega_0$) at the working distance was estimated to be 6 to 8 μm for the device on a 400- μm -thick MgO substrate, which is sufficiently small to allow efficient optical coupling with the meander nanowire area of 15 \times 15 μm^2 . This GRIN lens assembly technique can be used in combination with a substrate thinning process or can be used for front illumination with the advantage of demagnifying the optical spot down to 4 to 5 μm .

2.3 Optical Coupling Using Small Optics

Rather than using fusion-spliced GRIN lenses, other small optics have also been employed to focus light through the substrate. Using small optics provides considerable flexibility in optimizing the optical arrangement to demagnify the light from an SMF, multimode fiber, or a free-space optical beam. However, ensuring precise optical alignment at cryogenic temperatures is complicated by the larger optics and distances involved in this approach.

A straightforward, but burdensome, solution is to use cryogenic nanopositioners to perform the optical alignment *in situ*, based on feedback from the detector count rate. In a fiber-coupled system, this can be implemented either by moving an integrated optical assembly that includes the fiber and the focusing optics or by moving just the fiber

above a rigidly mounted focusing optic designed to image the optical mode onto the detector, often with some demagnification factor. Both approaches have similar complexity and can focus the light onto a detector that is smaller than the optical mode of the fiber. This is particularly important for multimode fibers, which can have core diameters that are larger than the 10 to 20 μm diameters of typical SNSPDs. Figure 3 shows an assembly that was used in the design of a multimode optical receiver.⁸ Results of a system that uses this approach for SMF coupling are described in Sec. 4.2.

Employing a multimode optical fiber for coupling to an SNSPD (as compared to SMF) confers an advantage for both classical and quantum optical photon-counting systems. For the former, it allows for the collection of light that may not have a uniform or stable phase front due to propagation through turbulence (as is commonly encountered in free-space systems) and, thus, cannot be focused to a small spot without requiring adaptive optics. For quantum optical systems, using a multimode system can potentially increase the flux of photons created from entangled or other nonclassical optical sources.

One challenge in coupling multiple spatial modes is to focus the light onto a small-diameter SNSPD. While one can employ free-space coupling of light to an SNSPD, this can be burdensome for most cryogenic systems, whereas fiber-coupled schemes offer flexible deployment and potentially reduced background light. Employing multimode fiber in such a system requires a careful tradeoff of the size of the receiving aperture, the number of modes supported by the fiber, focusing optics required for the SNSPD detector collection, and the acceptable background light coupled into the fiber.

Most SNSPDs are sensitive to polarization, and polarization maintenance in multimode fiber is not readily achieved in commercially available multimode fibers. To maintain multimode polarization, to date two approaches have been employed. The first is to engineer optical fiber—typically a polymer fiber—with extremely low birefringence.^{9,10} The second is to employ stress-inducing elements to create a large birefringence and create orthogonal modes of

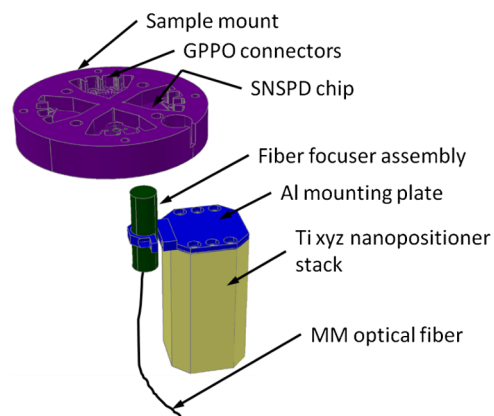


Fig. 3 Schematic layout for backside-illuminated SNSPD arrays using a cryogenic xyz nanopositioner stack with a multimode fiber coupled optical focusing assembly (only one of four nanopositioner stacks and focusing assemblies are shown in the figure). The sample mount holds four SNSPD arrays, and each array can have up to four SNSPD elements.

polarization preservation using panda-type stress rods of an elliptical core.⁸ Because the various modes experience different effective indices of refraction, the extinction will vary among the modes present in the fiber and its effectiveness will depend on the requirements of the system.

Finally, an emerging technique for optical coupling is lithographic alignment of a focusing optic on the opposite side of the wafer from the detectors. Microlenses that are etched in the substrate material can offer a relatively high numerical aperture, particularly in high-index substrate materials, such as silicon. The combination of the high numerical aperture and lithographic alignment allows efficient optical coupling to small-diameter detectors. Additionally, matching the microlens focal length to the substrate thickness produces a design that relaxes the alignment tolerances on the optical input, which could be coupled into the cryostat through a window or an optical fiber. Depending on the substrate and desired numerical apertures, microlenses with 50- to 200- μm diameters would likely be employed and could be arrayed with high fill factor, while providing space for electrical connections between elements of a detector array on the opposite side of the wafer. Consequently, with further development, microlenses may overcome the primary disadvantage of using a thick substrate by permitting a low-complexity approach to optical alignment.

3 Electrical Interfaces

In the circuit model for SNSPD operation developed in the early works on these devices,¹¹⁻¹³ the detector is represented as a variable resistor (hotspot) in series with an inductor (dominated by the kinetic inductance), and the readout circuit is viewed as a simple, dc-coupled impedance to ground. This model results in the simple detector dynamics described in Ref. 11, where the electrical behavior of the detector is purely inductive outside of the very short period when the wire has an electrical resistance and Joule heating plays a role. However, as described in Refs. 14 and 15, in nearly all SNSPD systems to date, the load seen by the detector is not simply resistive and independent of frequency as in this simple model, resulting in an effective nonlinear feedback, which couples the average count rate with the DE and, at extremely high count rates, can even drive the detector

into the latched state (where it becomes insensitive to photons and must be reset by turning the bias current down externally).¹⁵ To avoid this nonlinearity, one must operate at very low count rates of order ~ 20 times slower than τ_r^{-1} or below (where τ_r is the inductance-limited reset time of the device) or employ a readout approach that alleviates this undesirable feedback. Alternatively, higher count rates can be achieved using multielement SNSPDs,¹⁶ which can also enable limited photon-number resolution and single-photon imaging. One of the big challenges to realize the multielement SNSPDs is readout electronics. As the increased number of readout cables causes a significant heat load to the cryocooler and increased complexity, it is highly desirable to use cryogenic signal processing to alleviate the need for a separate cable for each detector element. In this section, approaches for removing the count-rate-dependent feedback and electrically addressing multiple, independent detector elements will both be described.

3.1 dc-Coupled Electrical Readouts

The circuit of Fig. 4(a) (Refs. 4 and 15) is used to present the SNSPDs with the most well-defined, wideband, resistive impedance possible. The gate electrode of a commercial high-electron-mobility transistor (HEMT) (Eudyna FHX45X) provides a wideband high impedance, which is shunted with a resistor R_L . The HEMT is operated in the usual common-source configuration, and its high gain and wide bandwidth effectively isolate the SNSPD from the electrical environment on the downstream side of its drain electrode. The SNSPD is tied to ground at dc, so both the drain and source of the HEMT must be biased in order to turn its channel on. Additionally, because the HEMT is a depletion-mode device, both of these voltages are positive: $V_D > V_S > 0$. To provide additional gain, a second cascaded, common-source stage is used and it is ac-coupled for ease of biasing. With this simple preamplifier, the nonlinear effect of Refs. 14 and 15 is completely removed, and the SNSPD behaves as expected based on independent measurements of its kinetic inductance and DE,^{4,15} as shown in Fig. 4(b).

The isolation provided by the preamplifier from the 50 Ω impedance of the subsequent readout electronics also makes it possible to independently adjust the load impedance

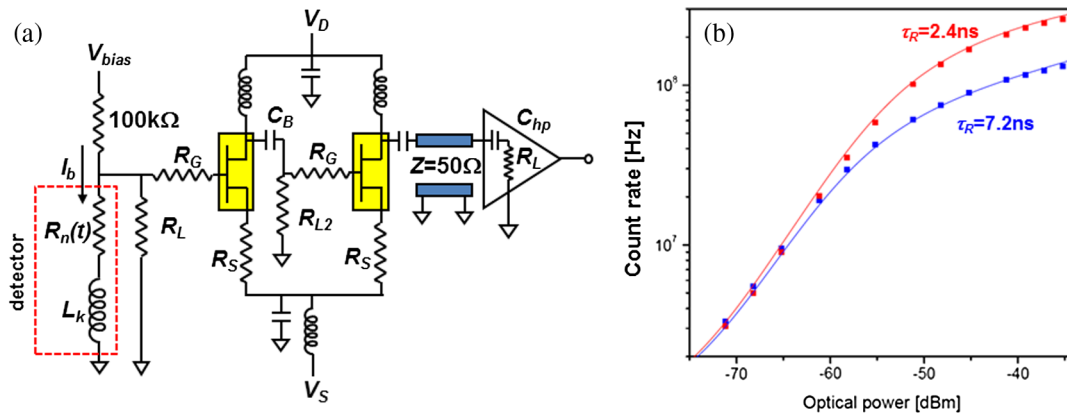


Fig. 4 (a) Electrical schematic of the cryogenic, wideband preamplifier for SNSPD readout that removes the ac-coupled feedback, which would otherwise prevent operation at high count rates. (b) Experimental data (squares) and simulated operation (lines) demonstrating proper operation of the SNSPDs at high count rates using two different values for the shunt resistance R_L .

seen by the SNSPD simply by changing R_L . As discussed in detail in Refs. 13 to 15, increasing R_L both decreases the reset time τ_R and increases the signal size; however, by decreasing the reset time, it also stabilizes the latched state of the detector at lower bias currents. Therefore, the optimal load impedance is obtained by increasing R_L until the detector is just beginning to latch at $I_b = I_C$ (i.e., the latching current decreases to I_C). Further speedup would make the highest DEs inaccessible, as the device would begin to latch at bias currents below I_C in the region where the highest DE would otherwise be obtained.

Although this circuit is typically operated under conditions where the power dissipation is only ~ 1 mW, it is still of critical importance to ensure that none of this power makes it to the SNSPD itself, but is instead removed by the cryogenic system. The same goes for any heat flux coming down the coaxial lines, which carry the wideband detector signals to room temperature. To this end, the circuit is constructed on an aluminum nitride substrate, with a patterned gold coplanar waveguide for the signal lines, which is itself reflow-soldered with pure indium to a copper heat sink. This provides excellent thermal anchoring such that no heating of the detector is observed (when compared to a purely passive readout) and a high density of detector channels can be realized. For example, 16 independent amplifier channels have been operated simultaneously to readout four independent four-element arrays, which were packaged in a single sample mount of ~ 5 cm diameter.⁸ Newer designs will incorporate arrays of twice this size or larger.

3.2 Semiconductor-Based Electrical Multiplexing

In a typical SNSPD readout circuit, the change in the impedance of the nanowire to several kilohms upon photon

absorption is detected by placing the nanowire in parallel with an amplifier, as shown schematically in Fig. 5(a). The critical current of the WSi nanowires is only of the order of a few microamperes, so it is advantageous (although not strictly necessary) to use a cryogenic amplifier circuit to improve the signal-to-noise ratio. As described earlier in this section, when the amplifier is ac coupled, a nonlinear interaction between the detector and the readout circuit gives rise to an artificially low saturation count rate,^{14,15} and it is necessary to implement a dc-coupled amplifier or to provide an alternative low-frequency current path to ground to prevent this saturation effect.

A scalable, low-cost cryogenic readout circuit based upon a commercially available SiGe radio frequency (RF) amplifier technology has been developed. A schematic is shown in Fig. 5(b). This circuit is operated at the 40-K stage of a pulse-tube refrigerator, and its overall in-band noise temperature is 90 K. The overall bandwidth of the circuit ranges from 10 MHz to 2 GHz. Note that while the amplifier is ac coupled, the nanowire is coupled to the amplifier input through a wideband 1:1 transformer, which passes the high-frequency components of the output pulse to the amplifier while maintaining a low-frequency current return path to ground. The detector bias current is added with a resistive network directly at the amplifier board, simplifying cryostat wiring in the case of a large number of detectors or a large SNSPD array.

As WSi SNSPDs must be operated below 2 K for optimum performance,³ they are typically operated using a low-temperature insert, such as a closed-cycle helium-4 or helium-3 refrigerator or adiabatic demagnetization refrigerator. As such systems have limited cooling power (on the order of 1 mW for a typical He-4 refrigerator), the high-bandwidth cryogenic interconnects between the nanowires

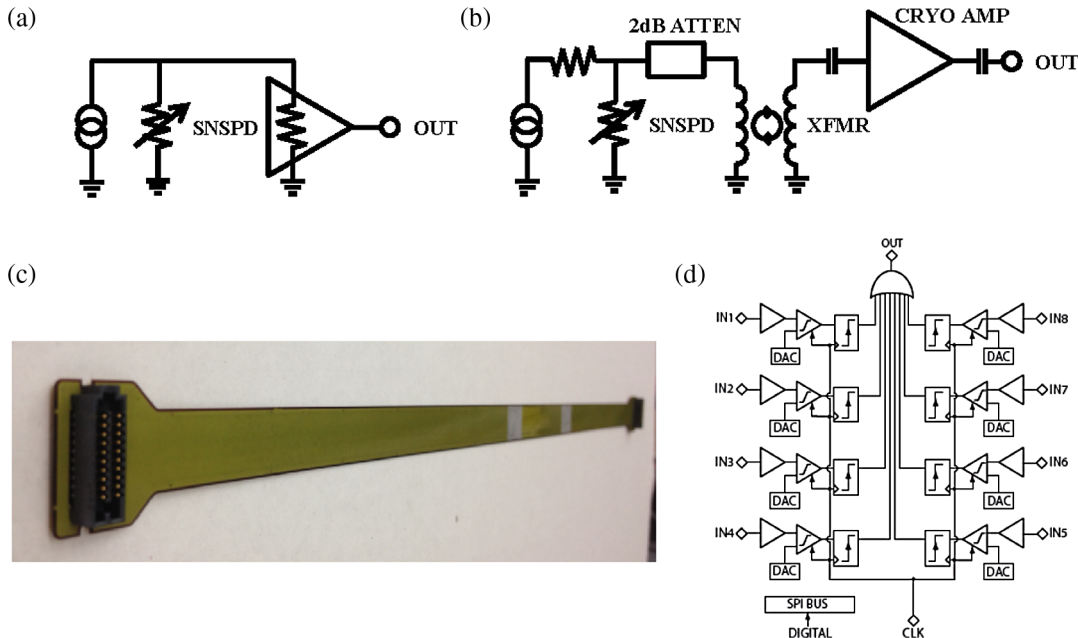


Fig. 5 (a) High-level schematic of a standard SNSPD readout circuit. The SNSPD is represented by the variable resistor. (b) Schematic of the transformer-coupled cryogenic amplifier circuit used in the WSi SNSPD readout. (c) Photograph of the 16-channel flex-print circuit used as a cryogenic interconnect between the detectors at 1 K and the amplifier circuits at 40 K. (d) Schematic of the monolithically integrated SiGe readout integrated circuit. Clock distribution, retiming, and monitor bus circuitry are not shown.

and the 40-K amplifier boards must be designed carefully. A small number of signal lines can be routed using standard stainless steel or CuNi coaxial cables, but this approach becomes unwieldy for large numbers of signals. As an alternative, a custom flex-print circuit patterned with high-bandwidth stripline waveguide traces can be used to route 16 SNSPD signals from a detector array at the cold stage to the amplifier circuits shown in Fig. 5(b). The flex circuits are based on a polyimide substrate metalized with brass traces for low thermal conductivity, with a Cu overlay on the amplifier end and a superconducting PbSn solder overlay on the detector end to improve the electrical performance. The total thermal load for 16 traces from 40 to 0.5 K was measured to be $88 \mu\text{W}$. An image of one of the flex circuits is shown in Fig. 5(c).

For many applications, it is advantageous to combine a large number of detector signals together to increase the maximum count rate from the entire system. Performing this signal combination at cryogenic temperatures greatly simplifies the cryostat wiring and reduces the complexity of the room temperature signal processing electronics, while allowing one to take advantage of low-noise cryogenic amplification. In collaboration with the University of Massachusetts, a monolithically integrated cryogenic readout integrated circuit (ROIC) based on low-power SiGe technology has been fabricated using the IBM BiCMOS8HP process. As shown in Fig. 5(d), the ROIC performs low-noise cryogenic amplification, analog-to-digital conversion, and eight-channel signal combination on a single chip, clocked from 2 to 8 GHz on the 40-K stage of a pulse-tube cryocooler. The ROIC has eight input channels for analog SNSPD signals. Each signal is boosted with a monolithically integrated cryogenic amplifier with 20 dB of gain and sent to a comparator with an independently programmable digital-to-analog converter (DAC) level. A flip-flop is then used to time the signals to a 2 to 8 GHz clock, and the signals are combined using a common-mode-logic OR gate. Programming for the DAC levels and DAC monitor bus is provided with a standard serial peripheral interface bus. Further details about the ROIC circuitry can be found in Ref. 17.

3.3 Superconductor-Based Electrical Multiplexing

A cryogenic readout using a single flux quantum (SFQ) logic circuit can also electrically address arrays of SNSPDs in a scalable way because it can operate with high speed and low power in a cryogenic environment.¹⁸ Signal conversion from the SNSPD outputs to the SFQ pulses has been demonstrated¹⁹ and the signal multiplexing function of the SFQ circuit has been implemented with the SNSPD in the same workspace on a 0.1-W GM cryocooler.²⁰ These demonstrations revealed that dc coupling with the SFQ readout is effective to prevent unstable operation of the SNSPD in the high bias-current region. Cross-talk-free operation of a four-element SNSPD array combined with the SFQ signal processing is shown in Fig. 6.²¹ The SFQ readout can also be effective as a preamplifier to reduce the timing jitter of the SNSPD when the conventional readout approach is limiting the achievable timing jitter. The current sensitivity of the SFQ readout circuit reached $8.2 \mu\text{A}$, and the resulting timing jitter via the SFQ preamplifier was 37 ps, while that for the conventional readout via the bias tee was 67 ps at a bias current to the SNSPD of $18 \mu\text{A}$.²² Since the number of

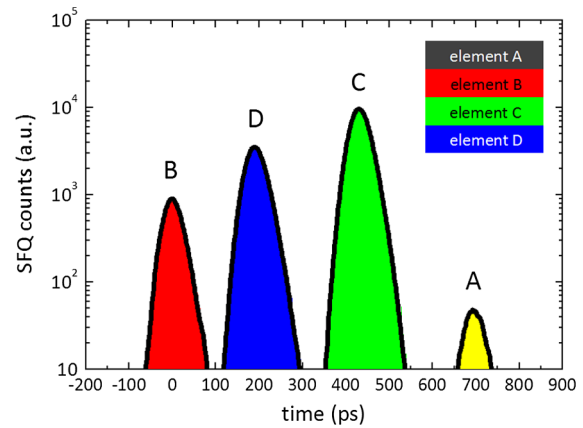


Fig. 6 Histogram of the time-correlated counts from the SFQ circuit when integrated with a four-element SNSPD (elements were arranged in a linear array, as shown in the inset, and, consequently, illuminated with different optical powers). Colored bar graphs indicate the histogram of the SFQ output when each element was biased individually. Black lines indicate the histogram for all elements when they were biased simultaneously. Electrical delays were intentionally introduced between the detector outputs to differentiate the four elements after multiplexing.

Josephson junctions required for the SFQ circuit described above is ~ 50 per pixel, the power required to drive an SFQ circuit is estimated to be a few microwatts per pixel, allowing signal processing for a few hundred pixels without significantly increasing the base temperature of 0.1-W GM cryocooler.

4 System Design and Performance

4.1 Single-Element NbTiN SNSPD System

The NbTiN SNSPD device structure is shown schematically in Fig. 7(a). The device consists of a 5-nm-thick, 100-nm-wide, and 60-nm spaced NbTiN meandering nanowire that covered a square area of $15 \times 15 \mu\text{m}$. The nanowire was fabricated on a 270-nm-thick thermally oxidized SiO_2 layer and covered by a 250-nm-thick SiO layer and a 100-nm-thick Ag mirror to enhance the absorption efficiency. The thickness of both the SiO_2 and the SiO layers were chosen to be $\lambda/4$ of 1550 nm, respectively.

This SNSPD device was installed in a GM cryocooler system using the optical interface described in Sec. 2.2 and an electrical interface consisting of a bias tee, low-noise current source, and a room-temperature amplifier, with and without a shunting resistor between the detector and the bias tee.⁵ The system DE, dark count rate (DCR), and full width at half maximum (FWHM) timing jitter of this packaged detector system is shown in Fig. 7(b). The I_{sw} of the device was $19.2 \mu\text{A}$, which was sufficient to achieve stable operation and short timing jitter. Although the system DE reached a maximum value of 77.3% when the bias current was set near I_{sw} , this bias condition may not be suitable for practical use because the DCR increased to $>10^4 \text{ c/s}$ [Fig. 7(b)]. However, the device could achieve high system DE, low DCR, and short timing jitter simultaneously for lower values of bias current. For example, the device showed a system DE of 74.0%, DCR of 100 c/s , and timing jitter of 68 ps [Fig. 7(c)] at a bias current of $18.0 \mu\text{A}$. The timing jitter values in the figure were observed with two

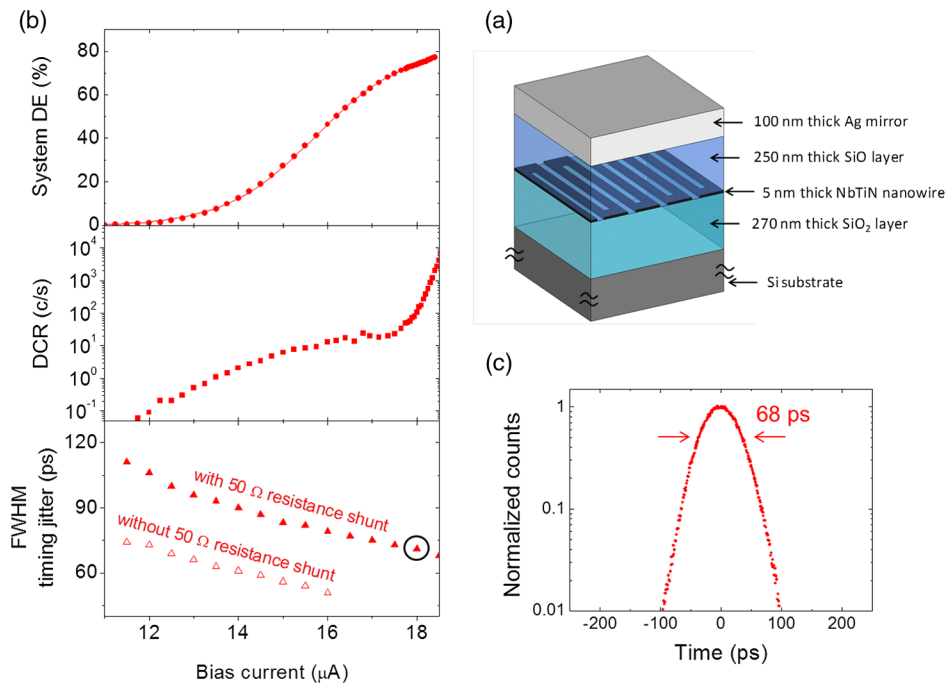


Fig. 7 (a) Schematic configuration of an Nbtin SNSPD on a thermally oxidized Si substrate. (b) System detection efficiency, dark count rate (DCR), and full width at half maximum timing jitter as a function of bias current for a device with 100-nm-wide and 60-nm spaced meandering nanowires installed into a Gifford-McMahon cryocooler system. (c) Histogram of timing jitter at a bias current of 18.0 μA with a 50-Ω shunting resistor [circled point in Fig. 2(b)].

conventional readout configurations: one had a 50-Ω resistor connected in parallel to the device and the other had no shunting resistor. The shortest timing jitter observed was 51 ps at a bias current of 16 μA without a shunting resistor. However, for higher values of bias current without the shunting resistor, the device latched into the normal state and stopped functioning. Although the 50-Ω shunting resistor is, thus, indispensable to achieve high system DEs in this conventional readout configuration, new approaches to the readout electronics that were discussed in Sec. 3 are designed to avoid the latching in the high bias-current region and would be effective in eliminating the need for the 50-Ω shunting resistor.

4.2 Multielement NbN SNSPD System

A second approach to operating SNSPDs with high system DE and high count rates used four-element NbN SNSPDs in two different types of closed-cycle cryogenic refrigerators. The first used a small-cooling-capacity GM cryocooler with a single SMF-28 input to a four-element SNSPD,⁴ and the second used a larger-capacity pulse-tube cryocooler with four multimode optical fibers (30 μm core, parabolic-graded index with a maximum NA of 0.2) coupled to four independent four-element SNSPDs. The larger-capacity cryocooler was designed for the ground receiver in the NASA-sponsored Lunar Laser Communication Demonstration to support data rates up to 622 Mb/s.^{8,23}

The design of the detectors used in both systems were identical and were fabricated from 5-nm-thick NbN films sputtered on a silicon wafer with a 260-nm-thick thermally grown SiO₂ coating, as shown in Fig. 8. The NbN film was patterned into detectors with 80-nm-wide wires on a pitch of 140 nm. A 250-nm-thick SiO_x spacer and a gold mirror were

deposited on top of the patterned NbN detector. The oxide layer thicknesses were chosen to optimize the absorption of 1550nm wavelength light in the SNSPD.

Light was coupled to the detectors through the back of the silicon substrate using an antireflection-coated optical fiber and an aspheric lens. For the SMF-28 fiber, the aspheric lens was fixed to the detector mount yielding a demagnification of 2. For the multimode fiber, a two-asphere lens assembly was fixed to the optical fiber providing a demagnification of ~4. In both cases, the optical fiber was manipulated with

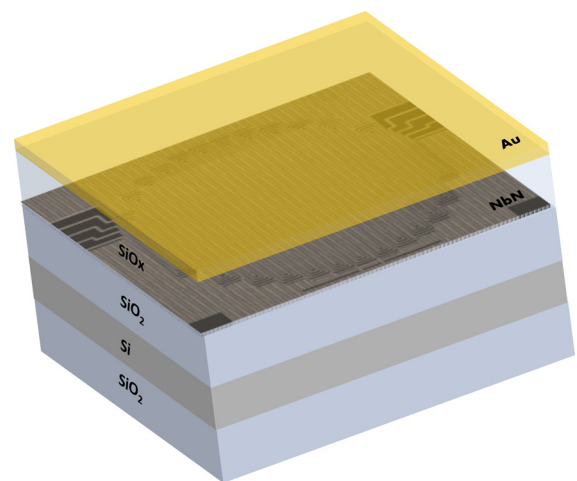


Fig. 8 Schematic of the NbN SNSPD cavity structure as illuminated through the silicon substrate, including a quarter-wave section of SiO₂ that acts as an antireflection coating, 230-μm-thick silicon substrate, another quarter-wave layer of SiO₂, the patterned, ~5-nm-thick NbN nanowires, a 250-nm-thick SiO_x layer, and a 120-nm-thick Au reflector.

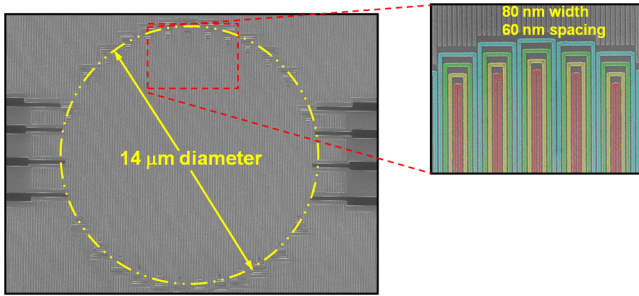


Fig. 9 Scanning electron micrograph of the interleaved four-element SNSPD pattern where the nanowire width was 80 nm with 60-nm spacing and the meander pattern covered a 14- μm -diameter circular area; inset shows the four interleaved nanowires that are colored to indicate the four electrically independent detectors.

an xyz nanopositioning stack (Attocube ANPx101/RES and ANPz101/RES) mounted inside the cryocooler on the second cooling stage to focus light onto the detector, as described in Sec. 2.3. The device consisted of an array of four interleaved SNSPDs patterned into a circle $\sim 14\ \mu\text{m}$ in diameter as shown in Fig. 9. Use of a detector array enabled a higher count rate for the given area, and the interleaved design ensured that all wires sampled the same optical mode. Note that at low counting rates, the interleaved array provided an approximate photon number resolution up to $n = 4$.¹⁶

The electrical signals from each of the four detector channels were read out using dc-coupled active cryogenic preamplifiers, described in Sec. 3.1, which enabled counting at rates for each wire approaching the inverse of the recovery time of a few nanoseconds⁴ (determined by the wires' kinetic inductance and the 160- Ω input impedance of the amplifiers,

the maximum value for these particular wires that did not induce detector latching below the critical current). The device performance for the small cryogenic systems with SMF-28 fiber coupling is shown in Fig. 10. The system DE can be further increased by (1) adding a better antireflection coating to the back side of the chip to eliminate the remaining $\sim 7\%$ reflectance from this surface, (2) increasing the absorption in the nanowires by optimizing the optical layers in the cavity and the NbN nanowire thickness and fill factor, and (3) using narrower or thinner nanowires to improve the internal efficiency in converting absorbed photons into detection events. Experimental studies and empirical models provide insight and have allowed progress in understanding the dependence that several parameters, including bias current, nanowire width, thickness, and superconducting material, have on this internal efficiency, but challenges remain in developing a more predictive and quantitatively accurate model based on independently measured material properties.

4.3 Si SNSPD System

A final recent SNSPD system exhibiting high DE is based on fiber-coupled amorphous WSi nanowires.⁵ A system detection efficiency (SDE), including optical-coupling losses, $>90\%$ was demonstrated in the wavelength range of $\lambda = 1520$ to 1610 nm; device DCR (DDCR, measured with the device shielded from any background radiation) ≈ 1 cps; system background count rate (SBCR, measured when the input fiber to the system was blocked by a shutter) ≈ 1 kcps (primarily due to blackbody radiation); timing jitter ≈ 150 ps FWHM; and reset time ≈ 40 ns.

Figure 11(a) shows the dependence of the SDE at $\lambda = 1550$ nm of the detector system reported in Ref. 3 on

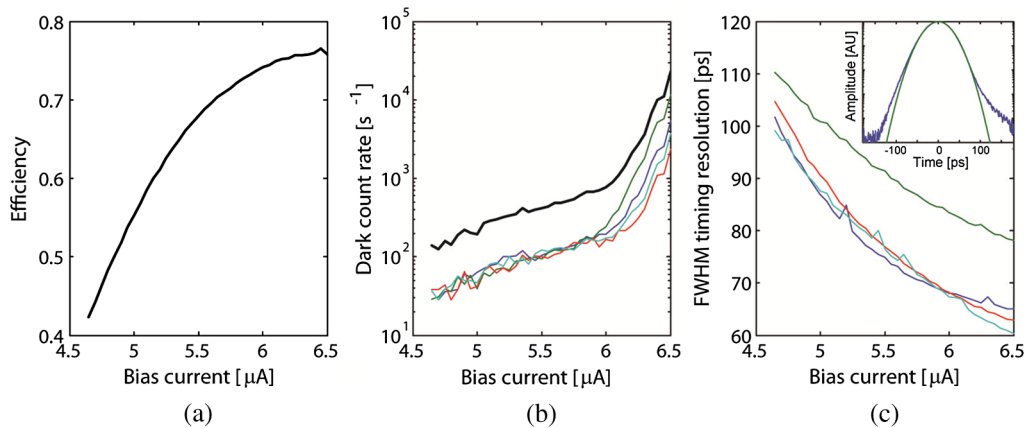


Fig. 10 (a) Total system detection efficiency (SDE) summed over all four detector channels. Variations of efficiency between devices were minimal, so only the sum is shown for clarity. The SDE exhibits a weak saturation near the critical current, implying high internal detection efficiency (note that this saturation is visible with the detection efficiency plotted on a linear scale). (b) DCR. The colored lines indicate the DCR per device, and the heavy black line is the total DCR summed over the four channels. The DCR decreases quickly away from the critical current and then displays a weaker bias-current dependence at lower currents. This behavior was also observed in Ref. 24–25, where the weaker dependence at lower currents arises from the fact that in this regime the DCR is dominated by background photons rather than true dark counts. (c) Timing resolution as a function of bias current for each of the four channels. The line colors correspond to the same detector channels as for part (b) of the figure. The timing jitter degrades as the bias current is lowered, which may be due to either a change in the timescales governing destruction of the superconducting state or the lower signal-to-noise ratio, or both. Variations in one or both of these is likely responsible for the difference in jitter between different channels. The inset shows a histogram of the electrical pulse arrival time relative to the optical pulse for one of the devices, where the absolute value on the horizontal axis has been (arbitrarily) centered on the measured distribution (adapted from Ref. 4).

the system background count rate for the polarization that minimized (SDE_{\min}) and maximized (SDE_{\max}) the count rate. Both the SDE_{\max} and the SDE_{\min} curves saturated at $SDE_{\max} \approx 93\%$ and $SDE_{\min} \approx 80\%$ for the system background count rate in the range $900 \text{ cps} < \text{SBCR} < 1400 \text{ cps}$. The measured value of SDE_{\max} was lower than the design value of the absorption of the SNSPDs ($>99\%$), which we attribute to several possible causes (see Ref. 3 for details): (1) fabrication imperfections; (2) our imperfect knowledge of the refractive index of the materials used in the optical stack; (3) coupling losses; and (4) the nonunity internal DE of the SNSPDs. Figure 11(b) shows the bias current (I_B) dependence of the DDCR and of the SBCR. The SBCR versus I_B curve had a sigmoidal shape similar to the SDE versus I_B curves and saturated at $\text{SBCR} \approx 1 \text{ kcps}$. The DDCR was $\leq 1 \text{ cps}$ for most of the bias range, which was

approximately two orders of magnitude lower than the DDCR of NbN SNSPDs of similar active area and fill factor.²⁵ The jitter of the detector system reported in Ref. 3 was 150 ps FWHM, which is higher than the values of 30 to 50 ps typically reported for NbN and NbTiN SNSPDs.² However, the system jitter was dominated by the electrical noise of the read-out circuit, rather than the intrinsic jitter of WSi SNSPDs. To improve the system jitter, WSi SNSPDs were recently fabricated with higher signal-to-noise ratio (SNR, the ratio of the amplitude of the photoresponse pulse and the FWHM of the electrical noise of the read-out) than that of the detector of Ref. 3. The SNR of WSi SNSPDs was increased by adopting larger and thicker nanowires and minimizing the current crowding at the bends of the meander,²⁶ increasing the switching current (I_{SW} , which was defined as the maximum current the device could

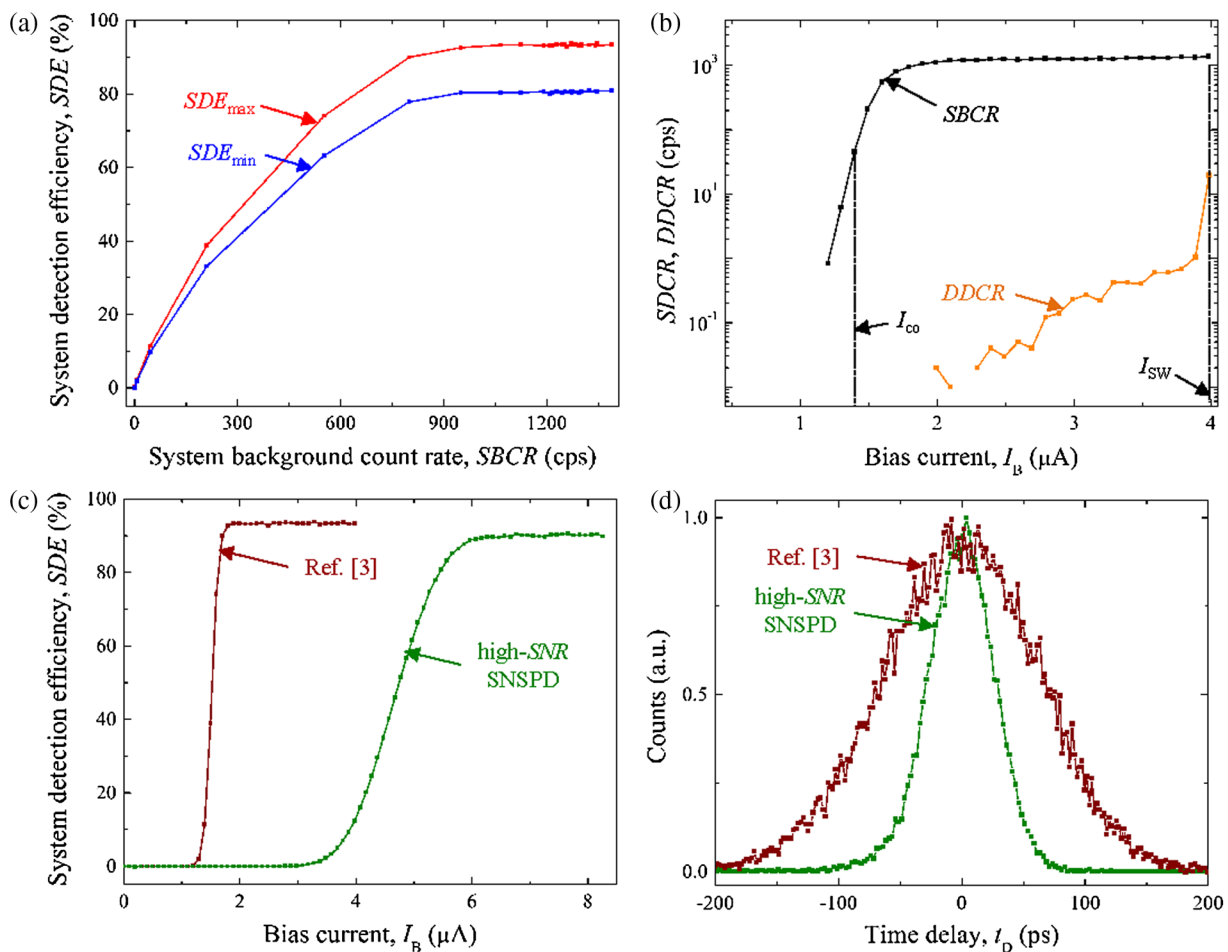


Fig. 11 (a) SDE versus system background count rate (SBCR) for two different polarizations of the light at $\lambda = 1550 \text{ nm}$. The SNSPD used was based on 4.5-nm-thick, 120-nm-wide WSi nanowires with 200-nm pitch. The SNSPD covered a square area of $15 \mu\text{m} \times 15 \mu\text{m}$. (b) SBCR and device DDCR versus I_B for the same device. The dashed lines indicate the cut-off current (I_{co} , which was defined as the bias current at the inflection point of the SDE versus I_B curve) and the switching current (I_{SW} , which was defined as the maximum current the device could be biased at without switching to the normal, nonsuperconducting state) of the device. (c) SDE_{\max} versus I_B for the high-SNR WSi SNSPD (green curve) and the SNSPD of Ref. 3 at $\lambda = 1550 \text{ nm}$. The high-SNR WSi SNSPD was based on 5-nm-thick, 135-nm-wide nanowires with 400-nm pitch. The active area of the SNSPD was circular with a diameter of $18 \mu\text{m}$. (d) Instrument response function (IRF) of the high-SNR WSi SNSPD biased at $I_B = 8.1 \mu\text{A}$ (green curve) and of the SNSPD of Ref. 3 biased at $I_B = 3.9 \mu\text{A}$ (red curve). The IRF at a particular I_B was obtained by calculating the histogram of the time delay (t_D) between the rising edge of the synchronization pulse of a mode-locked laser and the rising edge of the response pulse of the SNSPD. Each IRF was normalized by its maximum value.

be biased at without switching to the normal, nonsuperconducting state) of the detector and, consequently, the amplitude of the photoresponse pulses. Figure 11(c) shows the SDE_{\max} versus I_B curves of the high-SNR WSi SNSPD ($SDE \approx 88\%$, $I_{SW} \approx 8.2 \mu A$) and of the device of Ref. 3 ($SDE \approx 93\%$, $I_{SW} \approx 4 \mu A$). The plateau in the SDE_{\max} versus I_B curves is due to the saturation of the internal DE of the detector. Figure 11(d) shows the instrument response function (IRF) measured with the high-SNR WSi SNSPD (green curve) and with the device of Ref. 3 (red curve). The system jitter (defined as the FWHM of the IRF) improved from ~ 150 ps FWHM with the detector of Ref. 3 to ~ 60 ps FWHM with the high-SNR WSi SNSPD, which is comparable to the performance of NbN SNSPDs.

The DE of SNSPDs depends on polarization²⁷ and the degree of polarization dependence depends on the geometry and material properties of the nanowire. Quantitative modeling of the nanowire absorption suggests that the change in efficiency with polarization is predominately due to changes in absorption with polarization, and not due to a polarization dependence of the detection process itself

once a photon has been absorbed.²⁷ To further investigate the polarization dependence of the DE, the SNSPDs were embedded in an optical stack designed to have polarization-insensitive absorption at one particular wavelength. The polarization and wavelength dependence of SDE of these SNSPDs was characterized by mapping SDE onto the Poincaré sphere in the wavelength range of $\lambda = 1510$ to 1630 nm. Figures 12(a) and 12(b) show SDE (in color scale) as a function of the inclination ($2\theta_p$) and azimuth ($2\varepsilon_B$) angles of the polarization vector on the Poincaré sphere (we call this plot a Poincaré map of SDE) at $\lambda = 1520$ nm [Fig. 12(a)] and $\lambda = 1620$ nm [Fig. 12(b)]. The positions of the maxima and minima of the Poincaré maps were inverted at the two wavelengths, which implies that the SDE was polarization independent at a particular wavelength in the wavelength range of $\lambda = 1520$ to 1620 nm. Figure 12(c) shows the wavelength dependence of SDE at the polarization that maximized (orange squares) and minimized (violet squares) the SDE at $\lambda = 1520$ nm [Fig. 12(a)], which we named parallel and perpendicular polarization in analogy with Ref. 27. As shown in Fig. 12(c), the ratio

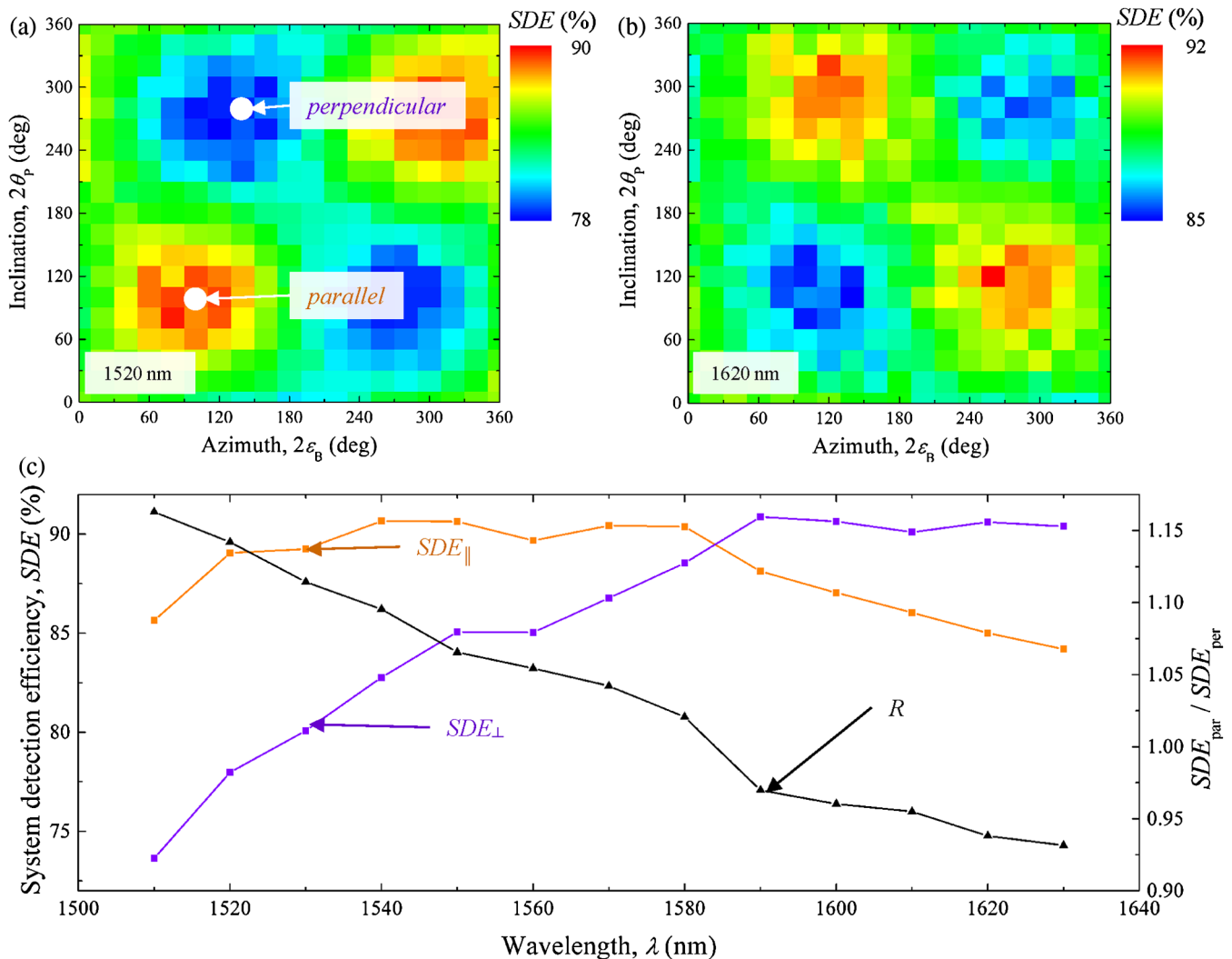


Fig. 12 (a) and (b) SDE (in color scale) versus the inclination ($2\theta_p$) and azimuth ($2\varepsilon_B$) angles of the polarization vector on the Poincaré sphere at (a) $\lambda = 1520$ nm and (b) $\lambda = 1620$ nm. (c) Wavelength dependence of SDE for parallel (SDE_{\parallel} , orange squares) and perpendicular polarization (SDE_{\perp} , violet squares), and of the ratio $R = SDE_{\parallel}/SDE_{\perp}$ (black triangles).

between the SDE for the parallel and perpendicular polarizations ($R = SDE_{\parallel}/SDE_{\perp}$, black triangles) changed from $R = 1.16$ at $\lambda = 1510$ nm to $R = 0.93$ at $\lambda = 1630$ nm, which suggests that SDE was polarization independent at a wavelength of 1580 nm $< \lambda < 1590$ nm.

For many applications, it is desirable to have a detector that is polarization insensitive over a certain spectral range. One approach to removing the polarization dependence over a certain wavelength range, while simultaneously increasing the signal-to-noise ratio of conventional SNSPDs, is by vertically stacking two WSi SNSPDs and electrically connecting them in parallel, forming a three-dimensional superconducting nanowire avalanche photodetector (3-D SNAP).²⁸⁻³⁰

While in prior work the sections of an SNAP were integrated side-by-side on a planar substrate,^{28,29} the sections of a 2-SNAP were more recently stacked vertically on top of each other.³⁰ Furthermore, because the two sections could be patterned independently, the nanowires in each section were patterned so that they were oriented at orthogonal angles

with respect to one another. The vertical stacking of orthogonal nanowire meanders connected electrically in parallel allowed us to achieve (1) a factor of ~ 2 higher signal-to-noise ratio than previously reported with WSi SNSPDs; (2) polarization-independent system detection efficiency over a ~ 100 -nm-wide wavelength range; and (3) system DEs $> 85\%$, comparable to the best results achieved to date with a planar WSi SNSPD.³

Figure 13(a) shows a diagram of the 3-D SNAP geometry, while Figs. 13(b) and 13(c) show scanning electron microscope images of the stacked nanowire meanders. The two nanowire meanders were separated by a $30 \mu\text{m} \times 30 \mu\text{m}$, 75-nm-thick square pad of hydrogen silsesquioxane, which served as the electrical insulator between the two SNSPDs. To increase the DE, the 3-D SNAP was embedded in a stack of dielectric materials to optimize absorption at $\lambda = 1550$ nm.

Figure 14(a) shows a plot of the dependence of the SDE at $\lambda = 1550$ nm of a 3-D SNAP on the system background count rate. This device was measured to have an SDE =

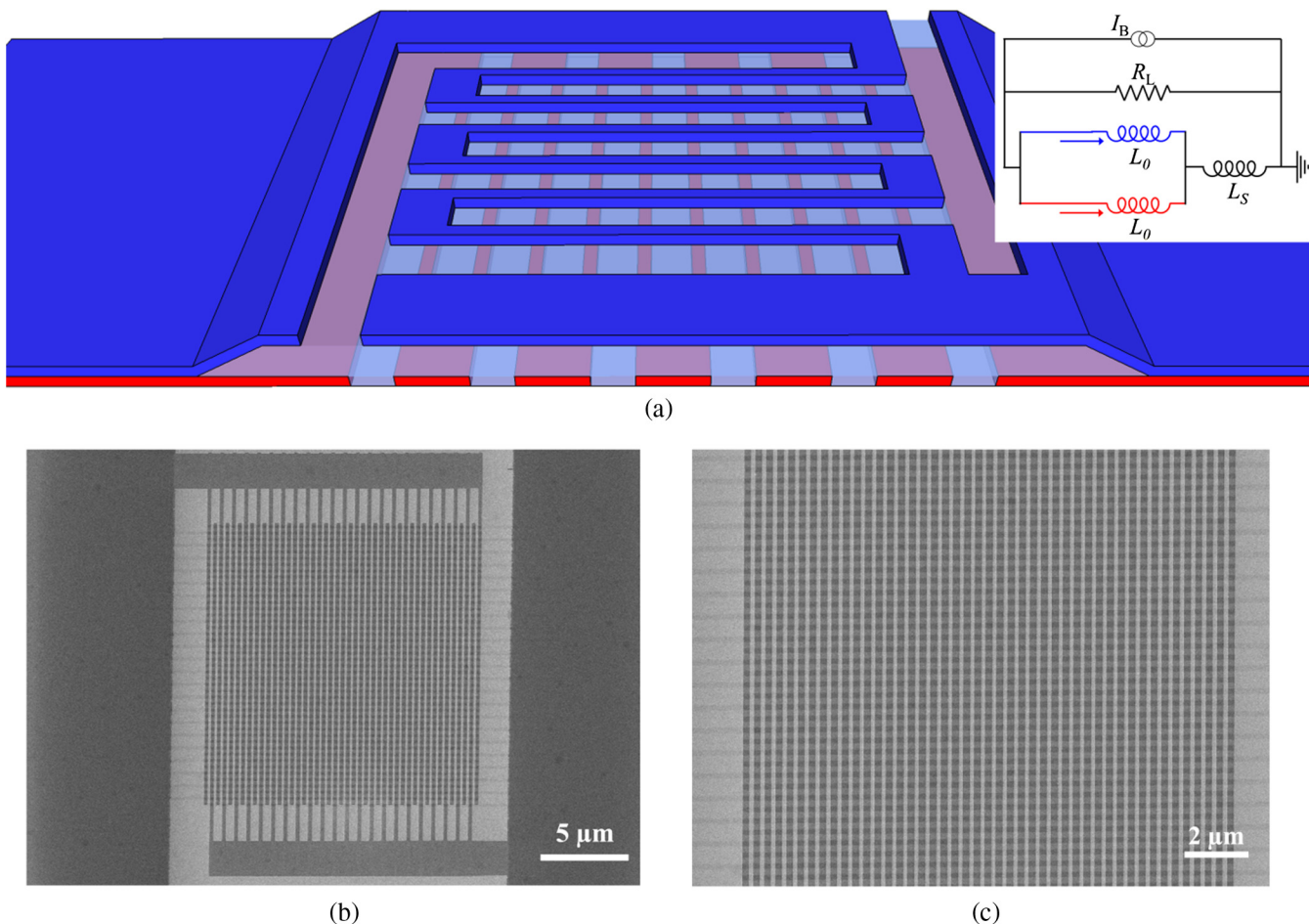


Fig. 13 (a) Three-dimensional (3-D) sketch of the 3-D superconducting nanowire avalanche photodetector (SNAP) (not to scale). The two meanders are connected electrically on the left and right sides of the sketch. The top and bottom layers of WSi are colored in blue and red, respectively, for clarity. The inset shows the electrical equivalent circuit diagram. The series inductor (L_S) is fabricated on-chip in the top layer (blue) of WSi away from the detector area and is not illustrated in the sketch. Each SNSPD has an inductance L_0 . I_B represents the bias current and R_L the load resistance. (b) SEM image of the 3-D SNAP. Wires (white-colored areas) in the top layer are oriented vertically, while wires in the bottom layer are oriented horizontally. The thin SiO_x insulating layer between meanders is transparent enough that the underlying wire layer can be resolved. (c) Higher magnification SEM image of the active area of the device.

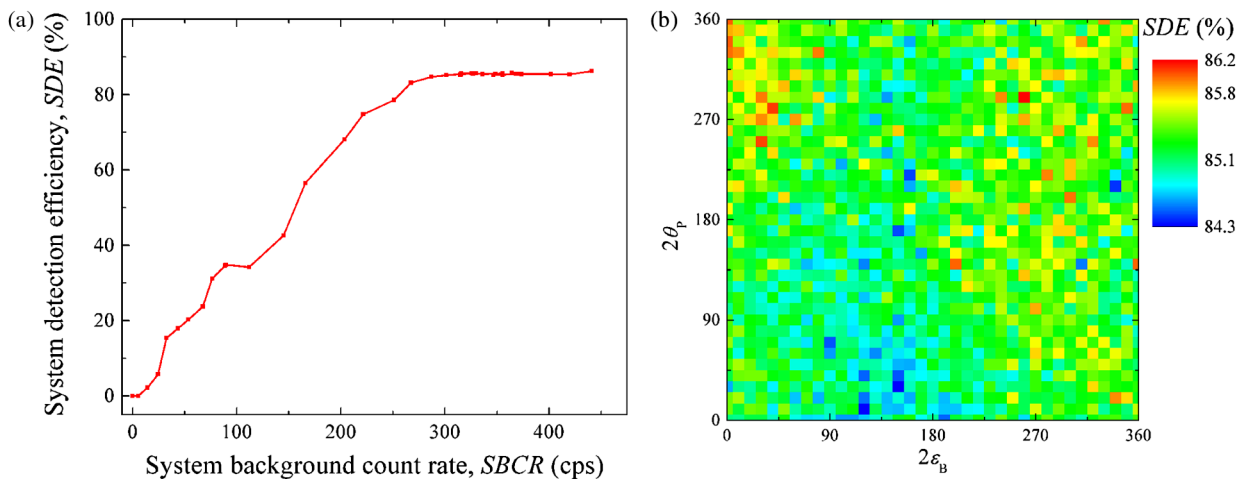


Fig. 14 (a) SDE versus SBCR curve for a 3-D SNAP. (b) Poincaré map of the SDE for a 3-D SNAP at 1560 nm.

$85.7 \pm 0.6\%$ together with an SBCR of ~ 400 cps. As expected, for two detectors connected in parallel, the switching current of $9.8 \mu\text{A}$ is approximately twice the switching current of a typical single-layer SNSPD ($\sim 5 \mu\text{A}$).

Although the larger signal-to-noise ratio is a benefit of the SNAP architecture, the primary motivation for stacking the two sections of the 3-D SNAP at orthogonal angles was to eliminate the polarization dependence of the SDE. Figure 14(b) shows a Poincaré map of SDE for the 3-D SNAP at a wavelength of 1560 nm. Variation of the SDE for the 3-D SNAP over the Poincaré sphere is $<2\%$ and is wavelength independent over an ~ 100 -nm range.

The extension of the SNAP nanowire architecture into three-dimensions represents a significant advancement in single-photon detector technology. The reduction of the polarization dependence of the SDE will enhance the overall DE in experiments where the light is unpolarized and will eliminate the need for polarization controllers and waveplates in experiments where the light is strongly polarized. Finally, stacking more than two layers may provide a route to obtaining DEs approaching 100% that are less wavelength dependent, which may be important for applications requiring high DE over a broad range of wavelengths.

5 Summary

In recent years, SNSPDs have matured from a promising detector technology to fully packaged systems that are being used in both research and deployed systems. This transition required a number of advances in both the optical and electrical interfaces as well as the overall design of the detector system. Many of the existing and emerging approaches to the optical and electrical interfaces have been described and contrasted to provide a broad view of the complexity and scalability of these techniques. Finally, a number of recently demonstrated high-performance systems were described to provide insight into the existing tradeoffs and the excellent performance that is achievable for applications requiring short-wave infrared single-photon detectors.

Acknowledgments

The MIT Lincoln Laboratory portion of this work is sponsored by the Assistant Secretary of Defense for Research

and Engineering under Air Force Contract FA8721-05-C-0002. Opinions, interpretations, conclusions, and recommendations are those of the author and are not necessarily endorsed by the U.S. government. Part of the research was carried out at the Jet Propulsion Laboratory, California Institute of Technology, under a contract with the National Aeronautics and Space Administration.

References

1. G. N. Gol'tsman et al., "Picosecond superconducting single-photon optical detector," *Appl. Phys. Lett.* **79**(6), 705–707 (2001).
2. C. M. Natarajan et al., "Superconducting nanowire single-photon detectors: physics and applications," *Supercond. Sci. Technol.* **25**, 1–16 (2012).
3. F. Marsili et al., "Detecting single infrared photons with 93% system efficiency," *Nat. Photonics* **7**, 210–214 (2013).
4. D. Rosenberg et al., "High-speed and high-efficiency superconducting nanowire single photon detector array," *Opt. Express* **21**(2), 1440–1447 (2013).
5. S. Miki et al., "High performance fiber-coupled NbTiN superconducting nanowire single photon detectors with Gifford-McMahon cryocooler," *Opt. Express* **21**(8), 10208–10214 (2013).
6. A. J. Miller et al., "Compact cryogenic self-aligning fiber-to-detector coupling with losses below one percent," *Opt. Express* **19**(10), 9102–9110 (2011).
7. S. Miki et al., "Multichannel SNSPD system with high detection efficiency at telecommunication wavelength," *Opt. Lett.* **35**(13), 2133–2135 (2010).
8. M. E. Grein et al., "Design of a ground-based optical receiver for the lunar laser communications demonstration," in *Int. Conf. on Space Optical Systems and Applications*, pp. 78–82, IEEE, Piscataway, New Jersey (2011).
9. R. Furukawa et al., "Waveguiding property of a plastic optical fiber fabricated using low-birefringence copolymer," *Jpn. J. Appl. Phys.* **46**(47), L1182–L1184 (2007).
10. R. Furukawa, A. Tagaya, and Y. Koike, "Modal analysis of a multi-mode polarization-maintaining plastic optical fiber fabricated using poly (methyl methacrylate/benzyl methacrylate) copolymer," *Appl. Phys. Lett.* **93**(10), 103303 (2008).
11. A. J. Kerman et al., "Kinetic-inductance-limited reset time of superconducting nanowire photon counters," *Appl. Phys. Lett.* **88**(11), 111116 (2006).
12. R. H. Hadfield et al., "Low-frequency phase locking in high-inductance superconducting nanowires," *Appl. Phys. Lett.* **87**(20), 203505 (2005).
13. J. K. W. Yang et al., "Modeling the electrical and thermal response of superconducting nanowire single-photon detectors," *IEEE Trans. Appl. Supercond.* **17**(2), 581–585 (2007).
14. A. J. Kerman et al., "Electrothermal feedback in superconducting nanowire single-photon detectors," *Phys. Rev. B* **79**(10), 100509 (2009).
15. A. J. Kerman et al., "Readout of superconducting nanowire single-photon detectors at high count rates," *J. Appl. Phys.* **113**(14), 144511 (2013).

16. E. A. Dauler et al., "Photon-number-resolution with sub-30-ps timing using multi-element superconducting nanowire single photon detectors," *J. Mod. Opt.* **56**(2–3), 364–373 (2009).
17. J. C. Bardin et al., "A high-speed cryogenic SiGe channel combiner IC for large photon-starved SNSPD arrays," in *Proc. IEEE Bipolar/BiCMOS Circuits and Technology Meeting*, pp. 215–218, IEEE, Piscataway, New Jersey (2013).
18. H. Terai, S. Miki, and Z. Wang, "Readout electronics using single-flux-quantum circuit technology for superconducting single-photon detector array," *IEEE Trans. Appl. Supercond.* **19**(3), 350–353 (2009).
19. H. Terai et al., "Demonstration of single-flux-quantum readout operation for superconducting single-photon detectors," *Appl. Phys. Lett.* **97**(11), 112510 (2010).
20. S. Miki et al., "Superconducting single photon detectors integrated with single flux quantum readout circuits in a cryocooler," *Appl. Phys. Lett.* **99**(11), 111108 (2011).
21. T. Yamashita et al., "Crosstalk-free operation of multi-element SSPD array integrated with SFQ circuit in a 0.1 W GM cryocooler," *Opt. Lett.* **37**(14), 2982–2984 (2012).
22. H. Terai et al., "Low-jitter single flux quantum signal readout from superconducting single photon detector," *Opt. Express* **20**(18), 20115–20123 (2012).
23. B. S. Robinson et al., "Overview of the lunar laser communications demonstration," *Proc. SPIE* **7923**, 792302 (2011).
24. T. Yamashita et al., "Temperature dependent performances of superconducting nanowire single-photon detectors in an ultralow-temperature region," *Appl. Phys. Express* **3**(10), 102502 (2010).
25. T. Yamashita et al., "Origin of intrinsic dark count in superconducting nanowire single-photon detectors," *Appl. Phys. Lett.* **99**(16), 161105 (2011).
26. J. R. Clem et al., "Geometry-dependent critical currents in superconducting nanocircuits," *Phys. Rev. B* **84**(17), 174510 (2011).
27. V. Anant et al., "Optical properties of superconducting nanowire single-photon detectors," *Opt. Express* **16**(14), 10750 (2008).
28. M. Ejrnaes et al., "A cascade switching superconducting single photon detector," *Appl. Phys. Lett.* **91**(26), 262509 (2007).
29. F. Marsili et al., "Single-photon detectors based on ultra-narrow superconducting nanowires," *Nano Lett.* **11**(11), 2048–2053 (2011).
30. V. B. Verma et al., "A three-dimensional, polarization-insensitive superconducting nanowire avalanche photodetector," *Appl. Phys. Lett.* **101**(25), 251114 (2012).

Eric A. Dauler received his SB, MEng, and PhD degrees in electrical engineering and computer science from the Massachusetts Institute of Technology, where he worked in the Quantum Nanostructures and Nanofabrication Group. He is currently an associate technology officer at MIT Lincoln Laboratory, where he has held several positions since 2001. His research interests include superconducting and

semiconductor-based single-photon detectors, quantum measurements and devices, optical communication, and fabrication of optoelectronic devices.

Matthew E. Grein received his BS degree (summa cum laude) in electrical engineering from Texas A&M University and his MS and PhD degrees in the same field from the Massachusetts Institute of Technology in the Ultrafast Optics and Quantum Electronics Group. He currently works in the Optical Communications Technology Group at MIT Lincoln Laboratory, and his research interests include optical communication, ultrafast fiber and semiconductor lasers, optical sampling techniques, quantum noise, and single-photon detectors.

Andrew J. Kerman received his PhD from Stanford University in 2002 in atomic physics and completed his postdoctoral research at Yale University and the Harvard/MIT Center for Ultracold Atoms in 2004. Currently, he is a member of the Quantum Information and Integrated Nanosystems Group at MIT Lincoln Laboratory, where he conducts research on superconducting and trapped-ion qubits, quantum information processing architectures and quantum simulation, quantum phase-slip devices, and superconducting nanowire single-photon detectors.

Francesco Marsili (Swiss Federal Institute of Technology of Lausanne, EPFL, 2009) is a microdevices engineer at the Jet Propulsion Laboratory (JPL), where he is developing arrays of superconducting nanowire single-photon detectors (SNSPDs) for deep space optical communications. Before joining JPL, he demonstrated photon number resolving superconducting detectors at EPFL, SNSPDs sensitive in the mid-IR at the Massachusetts Institute of Technology, and single-photon detection with near-unity efficiency in the near-IR at the National Institute of Standards and Technology.

Matthew D. Shaw is pursuing the development of tungsten silicide SNSPD arrays for applications in optical communication at JPL. Prior to joining JPL in 2011, he was a postdoctoral scholar in the Keith Schwab Group at Caltech. He received his BA in physics from Reed College in 2000, his MS in electrical engineering from Boston University in 2002, and his PhD in physics from the University of Southern California in 2009.

Biographies of the other authors are not available.